Chapter 13
Synthesis and Structures of Novel Solid-State Electrolytes

Ryoji Kanno, Genki Kobayashi, Kota Suzuki, Masaaki Hirayama, Daisuke Mori and Kazuhisa Tamura

Abstract Two classes of new materials possessing ion conductivity have been developed: a lithium ion conductor and a hydride ion conductor. Conventional perovskite and ordered rock-salt structures were adopted as frameworks for lithium migration, and electrochemically stable elements such as Al, Ga, Ta, and Sc were used in the materials to facilitate their use as low-potential negative electrodes. New compositions of $(Li_{0.25}Sr_{0.625}V_{(Li,Sr)0.125})(Ga_{0.25}Ta_{0.75})O_3$, and $Li_{0.9}Sc_{0.9}Zr_{0.1}O_2$ were found to be novel oxide-based lithium ion conductors. Oxyhydrides with K_2NiF_4-type structures were synthesized via a high-pressure synthesis method and their use in pure hydride ion conduction was demonstrated. The $La_{2-x-y}Sr_{x+y}LiH_{1-x+y}O_{3-y}$ oxyhydrides showed wide composition ranges of solid solution formation and the conductivity increased with anion vacancies or the introduction of interstitial hydride ions. The performance of an all-solid-state $TiH_2/o\text{-}La_2LiHO_3$ ($x = y = 0$, o: orthorhombic)/Ti cell provided conclusive evidence of pure H^- conduction.

Keywords Solid electrolyte · Hydride ion conductor · Lithium ion conductor · Material search

R. Kanno (✉) · K. Suzuki · M. Hirayama
Department of Chemical Science and Engineering, School of Materials and Chemical Technology, Tokyo Institute of Technology, Yokohama 226-8502, Japan
e-mail: kanno@echem.titech.ac.jp

G. Kobayashi
Institute for Molecular Science, Research Center of Integrative Molecular Systems (CIMoS), 38 Nishigonaka, Myodaiji, Okazaki, Aichi 444-8585, Japan

D. Mori
Department of Chemistry for Materials, Graduate School of Engineering, Mie University, Tsu 514-8507, Japan

K. Tamura
Synchrotron Radiation Research Center, Kansai Research Establishment, Japan Atomic Energy Agency, Sayo-Gun, Hyogo 679-5148, Japan

I. Tanaka (ed.), *Nanoinformatics*, https://doi.org/10.1007/978-981-10-7617-6_13

13.1 Novel Solid-State Electrolytes

Solid materials exhibiting purely ionic conduction are used as solid-state electrolytes in a wide variety of electrochemical devices and chemical sensors, with the corresponding charge carriers being specific ions such as H^+, Cu^+, Ag^+, Na^+, Li^+, F^-, and O^{2-}. The resulting charged ion flow in electrolytes creates an electric current that drives the device, the characteristics and performance of which are thus influenced by the nature of the charge carriers. Generally, in view of their small ionic radii, cations migrate easily in solid electrolytes, showing facile diffusion. For example, silver and copper ion solid electrolytes, such as $RbAg_4I_5$ and $Rb_4Cu_{16}I_7Cl_{13}$, show extremely high ionic conductivities of > 100 mS cm^{-1} at room temperature [1–3]. Moreover, the recently developed lithium ion conductors ($Li_{10}GeP_2S_{12}$, LGPS) have achieved room temperature conductivities of >10 mS cm^{-1} [4, 5], with Li-based all-solid-state batteries reported to exhibit exceptionally good power characteristics. On the other hand, newly developed materials such as hydride ion conductors have expanded the research field and the scope of available energy devices [6, 7]. In this section, we focus on Li^+ and H^- as charge carriers and describe the structural characteristics of the corresponding newly developed materials.

13.2 Lithium Ion Conductors

Lithium ion conductors continue to attract much attention owing to their practical applications in all-solid-state lithium batteries [5, 8]. A wide variety of such conductors exists (e.g., LISICON, perovskite, garnet, glass, glass ceramics, thio-LISICON, and LGPS), some of which were developed in the 1970s [4, 9–14]. For instance, LGPS-based materials ($\sigma > 10$ mS cm^{-1} at 25 °C) enable high-power operation of solid-state lithium batteries; this is an intrinsic merit of solid-state systems, in addition to their safety and reliability. However, sulfide-based solids are sensitive to atmospheric moisture. As a result, most current research focuses on oxide-based materials, in order to satisfy the requirements of practical applications and engineering processes.

Novel ion conductors are typically developed using three methods: (i) element substitution-based, (ii) structure-based, and (iii) composition-based material searches. Approach (i) relies on existing materials with ionic conductivity of the target charge carrier [15], which are amenable to tuning of their physical and electrochemical properties [16]. Therefore, although it is relatively easy to find new materials using this method, remarkable performance improvements are difficult to achieve. Approach (ii) is initiated by selecting a suitable crystal structure candidate for ion diffusion [6, 11], which can be complicated by the fact that the diffusion of the target ion in the selected structure has usually not been demonstrated.

Finally, approach (iii) is the most challenging, but also has the greatest potential to afford new materials with unique structures and properties. This approach starts with the selection of a suitable phase diagram [17]. Subsequently, materials corresponding to the chosen region in this diagram are synthesized and characterized; in certain cases, they exhibit unique structures and properties [4, 18]. In this chapter, some examples of material searches are introduced.

13.2.1 Novel Lithium Ion-Conducting Perovskite Oxides [15]

Lithium ion-conducting solids are key materials for all-solid-state lithium batteries, which, compared with conventional liquid electrolyte-based lithium batteries, exhibit improved energy density, stability, safety, and reliability. Among the solid electrolytes that have been developed, the oxide-based ones are among the most promising candidates, owing to their high ionic conductivities and good chemical stabilities over a wide range of operating temperatures [11, 19]. Lithium ion-conducting perovskites such as $La_{(2/3)-x}Li_{3x}TiO_3$ (which exhibits an ionic conductivity above 10^{-3} S cm^{-1} at room temperature) are considered to be particularly attractive [19]. However, the interfacial reduction of Ti^{+4} to Ti^{+3} during the electrochemical process or upon contact with lithium metal gives rise to undesirable electronic conduction. On this basis, novel perovskite-structured materials were examined, in typical example of an element substitution-based material search. As a result, the Li-Sr-Ta-*M*-O system (*M* = Al, Ga) was postulated to be ideal for achieving high ionic conductivity, with $(Li_xSr_{1-x})(M_{(1-x)/2}Ta_{(1+x)/2})O_3$ mixed oxides expected to exhibit superior characteristics owing to (i) the presence of largely non-reducible metals (Ta and Al/Ga) in their structures, (ii) the presence of a large cation (Sr) at the *A*-site, (iii) the limited distortion of BO_6 octahedra exhibited by Ta at the *B*-site, (iv) the presence of a small *B*-site cation (Al, Ga), and (v) the availability of controlled vacancies introduced by adjusting the concentration of the *B*-site cation. Thus, $(Li_xSr_{1-x})(M_{(1-x)/2}Ta_{(1+x)/2})O_3$ (*M* = Al, Ga) and $(Li_xSr_{1-x-y}V_{(Li,Sr)y})(Ga_{[(1-x)/2]-y}Ta_{[(1+x)/2]+y})O_3$ systems were synthesized by solid-state reactions involving Li-rich starting materials to obtain a single phase. These were subsequently subjected to electrochemical examination and crystallographic analysis by X-ray and neutron diffraction Rietveld analysis.

The temperature-dependent conductivities of $(Li_{0.2}Sr_{0.65}V_{(Li,Sr)0.15})(Ga_{0.25}Ta_{0.75})O_3$ ($x = 0.2$, $y = 0.15$) and $(Li_{0.25}Sr_{0.625}V_{(Li,Sr)0.125})(Ga_{0.25}Ta_{0.75})O_3$ ($x = 0.25$, $y = 0.125$) are shown in Fig. 13.1, with the corresponding activation energies (E_a) calculated as 35.04 and 34.64 kJ mol^{-1}, respectively. The comparable E_a values of these systems indicate that they both feature the same Li^+ conduction mechanism. The highest conductivity exhibited by the $(Li_{0.25}Sr_{0.625}V_{(Li,Sr)0.125})(Ga_{0.25}Ta_{0.75})O_3$ ($x = 0.25$, $y = 0.125$) sample equaled 1.85×10^{-3} S cm^{-1} at 250 °C, which was the highest value measured for Li-Sr-Ga-Ta-O perovskite materials. The structure of

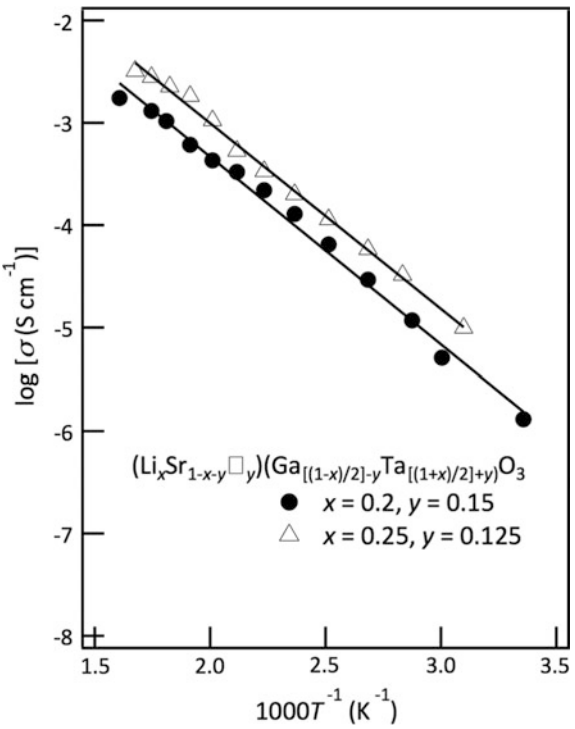

Fig. 13.1 Arrhenius plot showing the temperature-dependent conductivities of $(Li_xSr_{1-x-y}V_{(Li,Sr)y})(Ga_{[(1-x)/2]-y}Ta_{[(1+x)/2]+y})O_3$ with $x = 0.2$, 0.25 and $y = 0.125$, 0.15

this sample was determined by powder neutron diffraction and the obtained data were refined using a structural model of a cubic perovskite-type material with *Pm*-3 *m* symmetry.

Figure 13.2 shows the thermal ellipsoid structure model obtained by neutron Rietveld analysis and Table 13.1 summarizes the corresponding interatomic distances, revealing that the O–O distance of 2.79411 Å in $(Li_{0.25}Sr_{0.625}V_{(Li,Sr)0.125})(Ga_{0.25}Ta_{0.75})O_3$ was slightly larger than that determined for cubic perovskite-structured $Li_{0.5}La_{0.5}TiO_3$ (2.7358 Å). This increase was most likely due to substitution by the larger Sr^{2+} cation at the *A*-site, which is responsible for widening the bottleneck for lithium ion diffusion in the structure. The *A*–O distance of 2.79411 Å was larger than the calculated sum of the Li and O ionic radii of 2.32 Å (Li^+ (CN 8): 0.92 Å and O^{2-} (CN 6): 1.4 Å), making the Li cation more ionic in nature and, therefore, more mobile. The tolerance factor *t*, calculated based on the ionic radius of Sr^{2+} at the *A*-site, equaled 0.9855, which was close to unity and indicated an ideal cubic perovskite-type structure.

The increased ionic conduction was confirmed to result from the introduction of vacancies at *A*-sites. Average bond valence sum (BVS) values were calculated for each site of the perovskite structure using refined structural data, with the average BVS for *A*-sites equaling 1.98. The larger average BVS of $(Li_{0.25}Sr_{0.625}V_{(Li,Sr)0.125})(Ga_{0.25}Ta_{0.75})O_3$ compared with that of $La_{(2/3)-x}Li_{3x}TiO_3$ (0.95–1.57) [20]

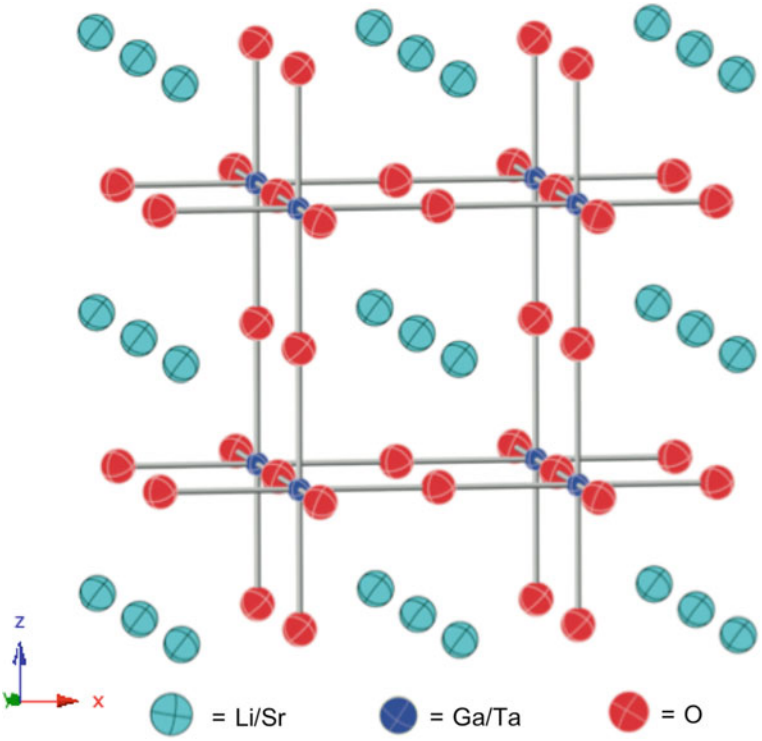

Fig. 13.2 Crystal structure model of $(Li_{0.25}Sr_{0.625}V_{(Li,Sr)0.125})(Ga_{0.25}Ta_{0.75})O_3$ based on neutron Rietveld analysis

Table 13.1 Selected bond distances for $(Li_{0.25}Sr_{0.625}V_{(Li,Sr)0.125})(Ga_{0.25}Ta_{0.75})O_3$

Distance/Å
A–O 2.79411(0)
B–O 1.97573(0)
A–*B* 3.42207(0)
O–O 2.79411(0)

A = Li and Sr, *B* = Ga and Ta

corresponded to the greater activation energy required for ion conduction in the former. Figure 13.2 shows the perovskite structure with thermal ellipsoids for each site, revealing their approximately isotropic thermal nature. The presence of vacancies in conjunction with Li ions at the *A*-sites suggests that Li diffusion proceeds according to the vacancy mechanism.

13.2.2 M-*Doped* $LiScO_2$ (M = *Zr, Nb, Ta) [21] as New Lithium Ion Conductors*

No material has yet been discovered that satisfies all requirements imposed on lithium ion conductors as solid electrolytes for battery applications (i.e., high ionic conductivity at room temperature, chemical stability, electrochemical stability, thermal stability, and low cost). This clearly indicates the need for further research efforts in this direction. Herein, we focus on $LiScO_2$, which has an ionic conductivity of 4×10^{-9} S cm^{-1} at 573 K. Although this value is not overly high, the above material is still attractive in view of its enhanced thermodynamic stability in contact with lithium metal [22].

As shown in Fig. 13.3, $LiScO_2$ has a fractional cationic ordered rock-salt structure exhibiting tetragonal $I4_1/amd$ symmetry [23], which has the potential to partially rearrange depending on the synthesis conditions and the doped element [24]. Although element doping is an effective method of increasing the ionic conductivities of solid lithium ion conductors such as $LiScO_2$, no corresponding investigations have been reported. Thus, in an attempt to improve the ionic conductivity of $LiScO_2$ by introducing lithium vacancies into its structure, this material was doped by $M = Zr^{4+}$, Nb^{5+}, and Ta^{5+}, and the crystal structures and ionic conductivities of the thus prepared $Li_{1-y}Sc_{1-x}M_xO_2$ were evaluated in detail.

$Li_{1-y}Sc_{1-x}M_xO_2$ ($M = Zr^{4+}$, Nb^{5+}, or Ta^{5+}; $x = 0.1$) were obtained via a solid-state reaction (sintering at 1073–1623 K for 1–12 h in air). Their impedance spectra and temperature-dependent conductivities are presented in Fig. 13.4. The

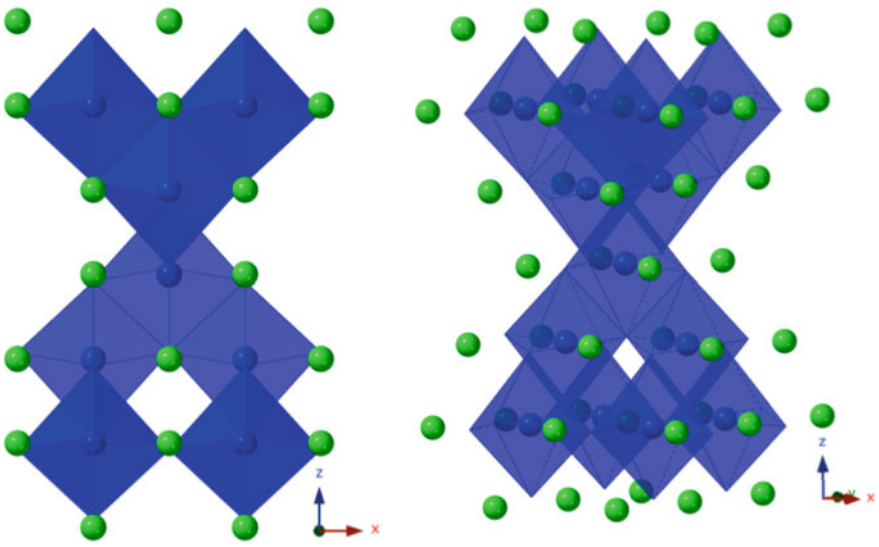

Fig. 13.3 Crystal structure of $LiScO_2$ [23], with blue octahedra and green spheres indicating ScO_6 and Li, respectively

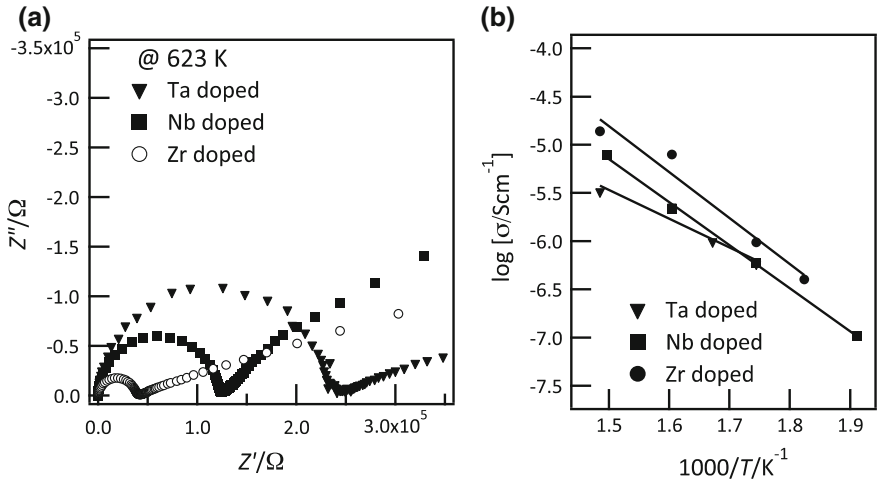

Fig. 13.4 **a** Representative impedance plots at 623 K and **b** Arrhenius plots showing the temperature-dependent conductivities of doped $Li_{1-y}Sc_{1-x}M_xO_2$ ($M = Zr^{4+}$, Nb^{5+}, or Ta^{5+})

conductivities were calculated from the corresponding impedance spectra, which comprised semicircles and spikes corresponding to contributions of the bulk and grain boundary and the electrode, respectively. The bulk and grain boundary contributions could not be separated and were therefore calculated together.

Resistances were calculated from the diameter of the aforementioned semicircles and used to determine conductivities. The diameters of these semicircles decreased upon doping, indicating the suitability of impedance spectroscopy to survey and evaluate ionic conductivities, with capacitance values corresponding to the observed semicircles being in the range of 10^{-10}–10^{-12} F. Table 13.2 summarizes the ionic conductivities and activation energies of $Li_{1-y}Sc_{1-x}M_xO_2$ ($x = 0.1$) at 573 K, along with the values previously reported for $LiScO_2$. All doped samples showed higher conductivities than the parent compound, owing to the formation of solid solutions upon aliovalent cation doping. Furthermore, this doping decreased the activation energies by more than 10%, indicating that the formation of lithium vacancies in the $LiScO_2$ lattice reduced the energy barrier of lithium diffusion.

Table 13.2 Ionic conductivities (573 K) and activation energies of $Li_{1-y}Sc_{1-x}M_xO_2$ ($M = Zr^{4+}$, Nb^{5+}, or Ta^{5+})

Doped element	Composition	Conductivity σ, S cm^{-1} @573 K	Activation energy E_a, kJ mol^{-1}
–	$LiScO_2$ [22]	4.2×10^{-9}	101
Ta	$Li_{0.8}Sc_{0.9}Ta_{0.1}O_2$	5.79×10^{-7}	57 ± 11
Nb	$Li_{0.8}Sc_{0.9}Nb_{0.1}O_2$	6.01×10^{-7}	85 ± 3
Zr	$Li_{0.9}Sc_{0.9}Zr_{0.1}O_2$	9.73×10^{-7}	88 ± 5

Table 13.3 Refined structural parameters of $LiScO_2$

Atom	Site	G	x	y	z	B, Å^2
Li	4*b*	1.0	0.0	0.25	0.375	2.0
Sc	4*a*	1.0	0.0	0.75	0.125	0.135(7)
O	8*e*	1.0	0.0	0.25	0.09895(3)	1.352(6)

Unit cell: tetragonal $I4_1/amd(141)$; $a = b = 4.1791(18)$ Å and $c = 9.3610(4)$ Å; $R_{wp} = 11.55$

Table 13.4 Refined structural parameters of $Li_{1-x}(Sc_{1-x}Zr_x)O_2$ ($x = 0.1$)

Atom	Site	G	x	y	z	B, Å^2
Li	4*b*	1 − [*g*(Zr)]	0.0	0.25	0.375	2.0
Sc	4*a*	1 − [*g*(Zr)]	0.0	0.75	0.125	0. 240(6)
Zr	4*a*	0.0968(7)	0.0	0.75	0.125	0.240(6)
O	8*e*	1.0	0.0	0.25	0.09793(3)	1.116 (6)

Unit cell: tetragonal $I4_1/amd(141)$; $a = b = 4.1804(16)$ Å, and $c = 9.4186(3)$ Å; $R_{wp} = 7.28$

Zr^{4+}-doped samples showed the highest ionic conductivities, with a maximum value of 9.73×10^{-7} S cm^{-1} observed at 573 K. In order to verify the changes in ionic conductivities caused by Zr^{4+} doping, the corresponding crystal structures were evaluated in detail.

Tables 13.3 and 13.4 summarize the refinement-determined structural parameters for $x = 0.0$ and $x = 0.1$, respectively. All diffraction peaks were indexed to the $I4_1/amd(141)$ space group with tetragonal symmetry, with the exception of reflections ascribed to impurities. The lattice parameters of $LiScO_2$ were determined as $a = b = 4.1791(18)$ Å and $c = 9.3610(4)$ Å, making them nearly identical to the reported values of $a = b = 4.182$ Å and $c = 9.318$ Å [23]. The lattice parameters calculated for $x = 0.1$ ($a = b = 4.1804(16)$ Å and $c = 9.4186(3)$ Å) were increased by doping with Zr^{4+}, with refinement results showing that 10% Zr^{4+} was doped at Sc^{3+} sites in the above structure, in agreement with the ratio of utilized reactants. Concomitantly, lithium vacancies were probably formed to maintain the charge balance in $LiScO_2$, since the doped Zr^{4+} ion has a higher charge than Sc^{3+}. These results demonstrate that the ionic conductivity of $LiScO_2$ was markedly improved by substitution with certain aliovalent cations, owing to the resulting lattice expansion and formation of lithium vacancies.

13.3 Development of Hydride Ion Conductors

Hydride ion conduction is particularly attractive, as H^- is similar in size to fast ionic conduction-suitable oxide and fluoride ions, while exhibiting strong reducing properties (standard H^-/H_2 redox potential = − 2.3 V), comparable to those of

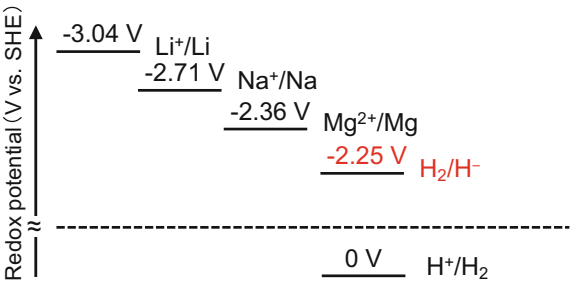

Fig. 13.5 Standard redox potentials of typical charge carriers, showing that the highly negative potential of H_2/H^- is similar to that of Mg^{2+}/Mg

Mg/Mg^{2+} (−2.4 V) (Fig. 13.5). Thus, hydride ion conductors may be applied in energy storage/conversion devices with high energy densities. To indicate a new direction for next-generation battery systems beyond lithium ion batteries and fuel cells, we herein focus on hydride ion conduction in solids.

Hydride ion conduction in CaH_2 was first described by Andresen et al. in 1977 [25], with similar reports on other materials following in later years [26–31]. However, experimental evidence of H^- conduction was not obtained until Irvine et al. determined the transport number of BaH_2 by electromotive force measurements in 2015 [7]. Although alkaline earth metal hydrides such as BaH_2 act as pure H^- conductors, they are also strong reducing agents. This complicates their use as solid electrolytes of energy devices, in which electrochemical stability to both oxidation and reduction is required. Indeed, these metal hydrides have not yet been applied to battery reactions. From the viewpoint of material design, the structural inflexibility of metal hydrides complicates the control of their lattice structure (which is required to create smooth transport pathways) and their conducting hydride ion content. Thus, little progress has been achieved in the development of H^- conductors. We have considered oxyhydrides, in which hydride and oxide ions share anion sublattices, as prospective hydride conductors with flexible anion sublattices. Known oxyhydrides include $A_2BH_xO_{4-x}$ (K_2NiF_4 structure; A = La, Ce, Nd, Pr, Sr; B = Co, V, Li; $0 < x \leq 1$), $Sr_3Co_2O_{4.33}H_{0.84}$ (Ruddlesden-Popper structure), $ATiO_{3-x}H_x$ (perovskite structure; A = Ba, Sr, Ca) [32–37], and $[Ca_{24}Al_{28}O_{64}]^{4+} \cdot 4H^-$ (mayenite structure) [38–40]. However, none of these materials display pure H^- conductivity, since hydride ions have been reported to act as electron donors in oxide-based materials [38–42], donating electrons to their lattice and thus causing electron conduction accompanied by a characteristic change in hydrogen charge from H^- to H^+. Indeed, perovskite- and mayenite-type oxyhydrides predominantly exhibit electron conduction caused by the dissociation of hydride ions into electrons and protons [33, 38–40, 43]. Taking this into consideration, preventing the above electron donation may be important for achieving pure H^- conduction in the oxide framework structure. Herein, we attempted to synthesize a series of K_2NiF_4-type oxyhydrides, $La_{2-x-y}Sr_{x+y}LiH_{1-x+y}O_{3-y}$ ($0 \leq x \leq 1$, $0 \leq y \leq 2$, $0 \leq x + y \leq 2$) featuring cation sublattices that contain cations that are more electron-donating than H^- and anion sublattices that allow flexible storage of H^-, O^{2-}, and vacancies.

13.3.1 Hydride-Conducting Oxyhydrides $La_{2-X-Y}Sr_{x+Y}H_{1-X+Y}O_{3-Y}$

Novel $La_{2-x-y}Sr_{x+y}LiH_{1-x+y}O_{3-y}$ oxyhydrides were synthesized by a high-temperature solid-state reaction in a cubic anvil cell [6] under high pressure to prevent the loss of light elements such as hydrogen, which can easily vaporize at high temperatures. The compositions and structures of $La_{2-y}Sr_yLiH_{1+y}O_{3-y}$ ($y = 0$, 1, 2) were determined by X-ray and neutron Rietveld analyses (Fig. 13.6). In La_2LiHO_3 ($x = y = 0$). The two apical sites of LiX_6 ($X = H^-$, O) octahedra were occupied only by O^{2-}, with the four in-plane apexes occupied by O^{2-} and H^-. These results indicate that highly charged cations, i.e., La^{3+} and Sr^{2+}, need to be surrounded by highly charged anions. $LaSrLiH_2O_2$ ($x = 0$, $y = 1$) was composed of tetragonal $(LiH_2)^-$ and $(LaSrO_2)^+$ layers alternately stacked along the c-axis, with the further increased hydride content of Sr_2LiH_3O resulting in the formation of $(Sr_2HO)^+$ layers. Considering the above series of compositions, it should be noted that there exists a K_2NiF_4-type H^-–free oxide, $La_2LiO_{3.5}$, in which the anion vacancies are randomly distributed in basal $(LiO_{0.75})^{0.5-}$ layers [44].

Remarkably, t-La_2LiHO_3 contains anion vacancies ($V_{(H,O)}$), which are best represented as $La_2Li(H_{0.53}O_{1.21}V_{(H,O)0.26})O_2$ and exhibit H^-, O^{2-}, and $V_{(H,O)}$ disorder at the axial sites of LiX_6 octahedra. By contrast, the orthorhombic phase, o-La_2LiHO_3, is stoichiometric, with H^- and O^{2-}located in axial anion sites. This symmetry change can be attributed to the order–disorder transition of H^- and O^{2-} in axial sites, both with and without vacancies. The crystal structures of the anion-deficient series, $La_{2-x}Sr_xLiH_{1-x}O_3$ and $La_{1-x}Sr_{1+x}LiH_{2-x}O_2$, were also determined by Rietveld analysis. Representative results obtained for

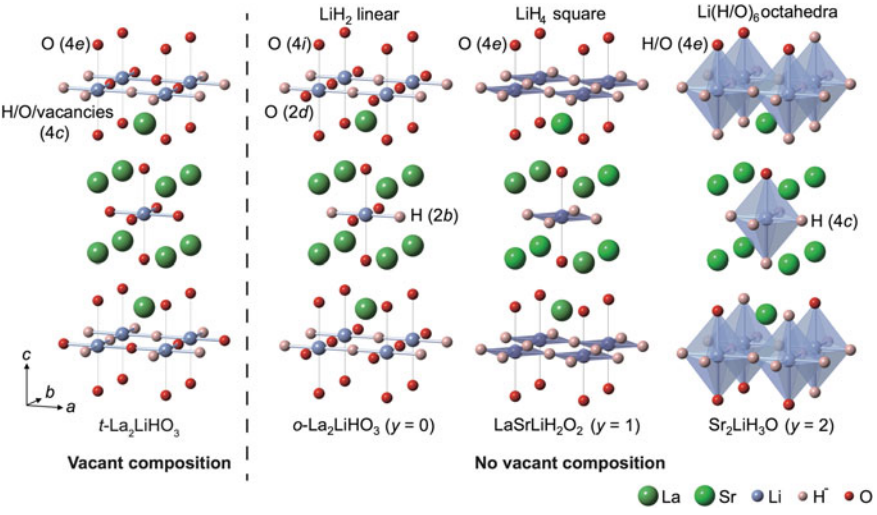

Fig. 13.6 Crystal structures of t-La_2LiHO_3 and $La_{2-y}Sr_yLiH_{1+y}O_{3-y}$ ($y = 0$, 1, 2)

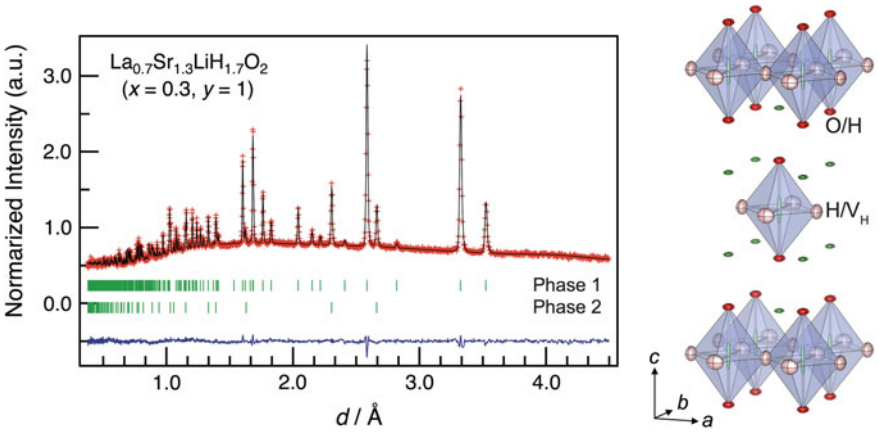

Fig. 13.7 Neutron Rietveld analysis of anion-deficient $La_{0.7}Sr_{1.3}LiH_{1.7}O_2$ ($x = 0.3$, $y = 1$)

$La_{0.7}Sr_{1.3}LiH_{1.7}O_2$ ($x = 0.3$, $y = 1$) are shown in Fig. 13.7 and Table 13.5. The H and O occupancy parameters were calculated as $g_{H1} = 0.938(2)$, $g_{H2} = 0.118(3)$, and $g_{O1} = 0.882(3)$, leading to a composition of $La_{0.7}Sr_{1.3}Li(H_{1.88}V_{(H)0.12})H_{0.24}O_{1.76}$. Thus, doping resulted in the generation of vacancies in the LiH_4 plane and caused H^-/O^{2-} anion mixing at apical sites.

The valence states of all constituent atoms in La_2LiHO_3, $LaSrLiH_2O_2$, and Sr_2LiH_3O were determined by valence charge integration over the corresponding Voronoi cells (Table 13.6). The valences of hydrogen and oxygen in all materials were estimated at approximately –0.8 to –1.0 and –1.3 to –1.6, respectively, indicating that these elements were present as H^- and O^{2-}. Electronic density of states calculations corroborated the presence of hydride ions (Fig. 13.8), with their localized electrons located between approximately 0 and –5 eV below the Fermi level, confirming the ionic nature of the Li–H^- bond.

13.3.2 Hydride Ion Conductivity of $La_{2-X-Y}Sr_{x+Y}H_{1-X+Y}O_{3-Y}$

The ionic conductivities of $La_{2-x-y}Sr_{x+y}LiH_{1-x+y}O_{3-y}$ were examined by impedance measurements. The Arrhenius plots of conductivities are shown in Fig. 13.9. In the case of $La_{2-y}Sr_yLiH_{1+y}O_{3-y}$ ($x = 0$), conductivity increased with increasing H^- content, with the highest value of 3.2×10^{-5} S cm^{-1} at 573 K observed for Sr_2LiH_3O ($y = 2$) (Fig. 13.9a). Thus, introduction of hydride ions into the anion sites of the K_2NiF_4 structure improved ionic conductivity, confirming that these ions were primary charge carriers. Conduction was further facilitated by the introduction of vacancies, indicating that structural defects can affect ionic diffusion, as can be seen for $La_{2-x}Sr_xLiH_{1-x}O_3$ ($y = 0$) and $La_{1-x}Sr_{1+x}LiH_{2-x}O_2$ ($y = 1$),

Table 13.5 Rietveld refinement results for $La_{0.7}Sr_{1.3}LiH_{1.7}O_2$ ($x = 0.3$, $y = 1$)

Phase 1: $La_{0.7}Sr_{1.3}LiH_{1.7}O_2$									
Atom	Site	g	x	Y	z	U_{11} =/Å^2	U_{22}/Å^2	U_{33}/Å^2	U/Å^3
La(1)	4*e*	0.354	0	0	0.35620 (9)	0.0072 (4)	0.0072 (4)	0.0045 (5)	0.0062 (3)
Sr(1)	4*e*	$1 - g_{La(1)}$	0	0	$= z_{La(1)}$	$= U_{11\ La(1)}$	$= U_{22\ La(1)}$	$= U_{33\ La(1)}$	$= U_{La(1)}$
Li(1)	2*a*	1	0	0	0	0.0037 (19)	0.0037 (19)	0.0352 (5)	0.0142 (6)
H(1)	4*c*	0.938 (2)	0	0.5	0	0.0258 (18)	0.0086 (14)	0.0090 (15)	0.0145 (6)
O(1)	4*e*	0.882 (3)	0	0	0.17138 (13)	0.0126 (8)	0.0126 (8)	0.0035 (9)	0.0096 (4)
H(2)	4*e*	0.118 (3)	0	0.5	0	$= U_{11\ O(1)}$	$= U_{22\ O(1)}$	$= U_{33\ O(1)}$	$= U_{O(1)}$
Unit cell: tetragonal *I*4/*mmm*, $a = 3.65672(4)$, $c = 13.3066(2)$ Å									
Phase 2: Li_2O									
Atom	Site	*g*	*x*	*y*	*z*	U/Å^2			
Li(1)	8*c*	1	0.25	0.25	0.25	0.0028(3)			
O(1)	4*a*	1	0	0	0	0.0049(5)			
Unit cell: cubic *Fd*-3 *m*, $a = 4.61290(11)$ Å									
$R_{wp} = 1.92$, $R_p = 1.47$, $R_e = 3.12$, $S = 1.63$, $R_B = 5.63$, $R_F = 5.21$									

Table 13.6 Valence states of elements in $La_{2-y}Sr_yLiH_{1+y}O_{3-y}$ ($y = 0$, 1, 2) derived from valence charge integrations over Voronoi cells, with (ax) and (ap) representing axial and apical anion sites, respectively

La_2LiHO_3 ($y = 0$)		$LaSrLiH_2O_2$ ($y = 1$)		Sr_2LiH_3O ($y = 2$)	
Atom	Valence	Atom	Atom	Atom	Valence
La	2.57	La	2.57	Sr (1)	1.8
Li	0.27	Sr	1.68	Sr (2)	1.69
H (ax)	–1.00	Li	0.43	Li	0.44
O (ax)	–1.26	H (ax)	–0.87	H (ax)	–0.80
O (ap)	–1.57	O (ap)	–1.47	H (ap)	–0.97
				O (ap)	–1.36

with conductivities of up to 2.1×10^{-4} S cm^{-1} observed for $La_{0.6}Sr_{1.4}LiH_{1.6}O_2$ at 590 K (activation energy ~ 68.4 kJ mol^{-1}) (Fig. 13.9b, c).

To further identify the nature of the charge carriers, the electrical conductivity of $La_{0.6}Sr_{1.4}LiH_{1.6}O_2$ ($x = 0.4$, $y = 1.0$) was evaluated by the Hebb-Wagner polarization method [45] at 480 and 590 K using an asymmetric (–) Pd/$La_{0.6}Sr_{1.4}LiH_{1.6}O_2$/Mo (+) cell, with the total electrical conductivities (electrons + holes) at the irreversible Mo-electrolyte interface (2.9×10^{-8} and 4.1×10^{-7} S cm^{-1}, respectively) showing that $La_{0.6}Sr_{1.4}LiH_{1.6}O_2$ is a purely ionic conductor (Fig. 13.10 and Table 13.7).

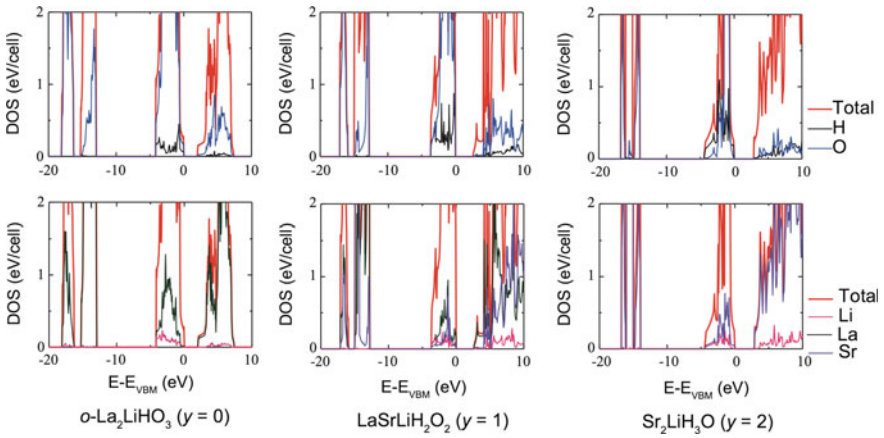

Fig. 13.8 Electronic densities of states for $La_{2-y}Sr_yLiH_{1+y}O_{3-y}$ ($y = 0$, 1, 2) determined by first principles calculations

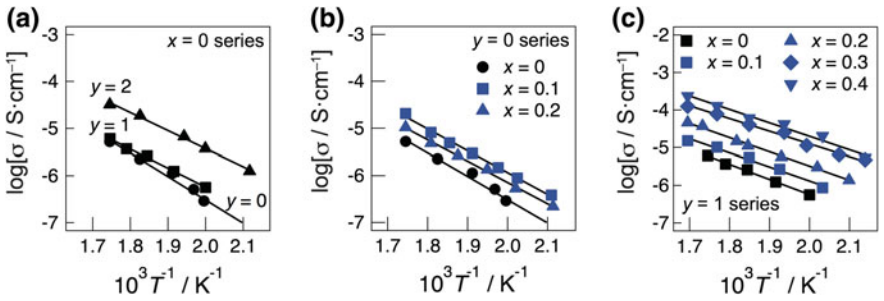

Fig. 13.9 Temperature-dependent ionic conductivities of $La_{2-x-y}Sr_{x+y}H_{1-x+y}O_{3-y}$. **a** $La_{2-y}Sr_yLiH_{1+y}O_{3-y}$ ($x = 0$, $y = 0$, 1, and 2) with a fixed cation/anion ratio of $(A_2B)/X_4$, where A, B, and X are La(Sr), Li, and O(H), respectively. Anion-deficient series: **b** $La_{2-x}Sr_xLiH_{1-x}O_3$ ($y = 0$, $0 \leq x \leq 0.2$) and **c** $La_{1-x}Sr_{1+x}LiH_{2-x}O_2$ ($y = 1$, $0 \leq x \leq 0.4$)

13.3.3 Development of Electrochemical Devices Based on Hydride Ion Conduction

To verify the occurrence of H^- conduction in $La_{2-x-y}Sr_{x+y}LiH_{1-x+y}O_{3-y}$, we constructed a Ti/*o*-La_2LiHO_3/TiH_2 all-solid-state cell and subjected it to galvanostatic discharge, with an electrode configuration (powdered mixture of electrode and electrolyte materials) similar to that previously used in an all-solid-state lithium battery [46]. Figure 13.11a shows the discharge curve of the cell, revealing a constant discharge current of 0.5 μA at 300 °C. Moreover, the cell showed an initial open circuit voltage of 0.28 V, which was consistent with the theoretical value calculated from the standard Gibbs energy of formation of TiH_2 [47]. During

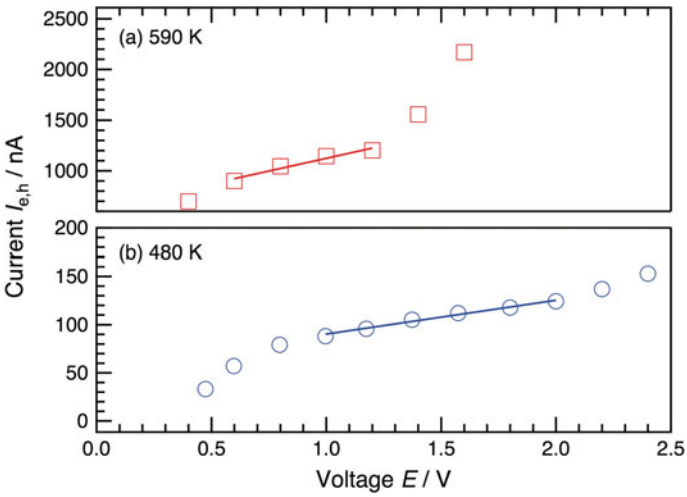

Fig. 13.10 Hebb-Wagner polarization curves of the (–) Pd/$La_{0.6}Sr_{1.4}LiH_{1.6}O_2$/Mo (+) cell at **a** 590 K and **b** 480 K

Table 13.7 Partial conductivities (σ) and transference numbers (t) at the irreversible Mo/$La_{0.6}Sr_{1.4}LiH_{1.6}O_2$ interface of the asymmetric (–) Pd/$La_{0.6}Sr_{1.4}LiH_{1.6}O_2$/Mo (+) cell at different temperatures. Subscripts e and h denote electrons and holes, respectively

	480 K	590 K
$(\sigma_e + \sigma_h)$/S cm^{-1}	2.9×10^{-8}	4.1×10^{-7}
σ_{H-}/S cm^{-1}	9.7×10^{-6}	2.1×10^{-4}
t_{e+h}	3.0×10^{-3}	2.0×10^{-3}
t_{H-}	1.0	1.0

the electrochemical reaction, the cell voltage rapidly dropped from 0.28 to 0.06 V and then gradually decreased to 0.0 V. The initial steep drop corresponded to an increase in hydride ion content at the anode, owing to the following constant current discharge reaction:

$$Ti + xH^- \rightarrow TiH_x + xe^-$$

with the cathode reaction represented as:

$$TiH_2 + xe^- \rightarrow TiH_{2-x} + xH^-$$

The occurrence of these discharge reactions was confirmed by analysis of the produced phases. Figure 13.11b shows the synchrotron X-ray diffraction patterns of the cathode, electrolyte, and anode materials before and after the reaction. The absence of any variation in the diffraction patterns of the electrolyte indicates that the La_2LiHO_3 electrolyte was stable in contact with the Ti and TiH_2 electrodes

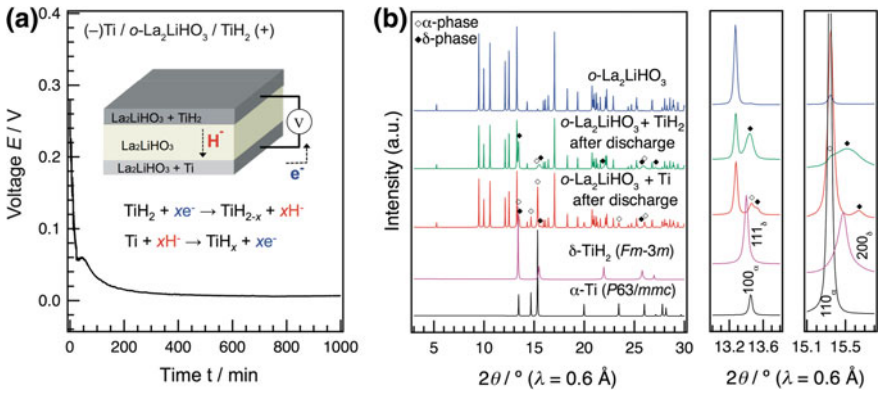

Fig. 13.11 All-solid-state cell fabricated for verification of H^- conduction in $La_{2-x-y}Sr_{x+y}LiH_{1-x+y}O_{3-y}$. **a** Discharge curve for a Ti/*o*-La_2LiHO_3/TiH_2 solid-state battery, with the inset showing a schematic illustration of the cell and the proposed electrochemical reaction. **b** X-ray diffraction patterns of electrolyte (*o*-La_2LiHO_3), cathode (TiH_2 + *o*-La_2LiHO_3), and anode (Ti + *o*-La_2LiHO_3) materials after the reaction; the two right panels show expanded ranges of 13–13.8° and 15.1–15.8°

during the reaction. Conversely, phase changes were observed for the cathode and anode materials, as expected from the Ti-H phase diagram [47], where the δ-TiH_2 (*Fm* $\bar{3}$ m) phase releases hydrogen and is transformed into α-Ti (*P*6_3/*mmc*), passing through a two-phase (α-TiH_b + δ-TiH_{2-a}) coexistence region found below ~ 573 K. In the case of the cathode, additional diffraction peaks corresponding to species with *P*6_3/*mmc* symmetry were detected, and the signals of TiH_2 shifted to a higher angle, indicating that the release of hydrogen from TiH_2 induced lattice shrinkage. In the case of the anode, peaks corresponding to species with *Fm* $\bar{3}$ m symmetry were detected. Thus, the results indicate that during the electrochemical reaction, hydride ions were released from the TiH_2 cathode and diffused into the Ti anode through *o*-La_2LiHO_3. The present success in the construction of an all-solid-state electrochemical cell exhibiting H^- diffusion confirms not only the ability of oxyhydrides to act as H^- solid electrolytes, but also the possibility of developing electrochemical solid devices based on H^- conduction.

13.3.4 Ambient-Pressure Synthesis of H^--Conductive Oxyhydrides

The abovementioned high-pressure method is efficient for synthesizing oxyhydrides, owing to its ability to inhibit hydrogen desorption from the starting materials during sintering. However, in order to apply H^- conductors to electrochemical devices, a simple synthetic protocol needs to be established for oxyhydrides, in parallel with the development of highly H^--conductive novel materials. Here, we

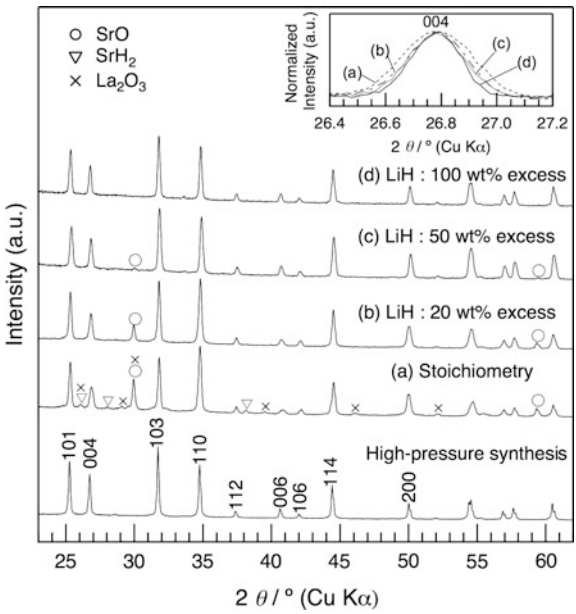

Fig. 13.12 X-ray diffraction profiles of $LaSrLiH_2O_2$ synthesized using various amounts of LiH: **a** stoichiometric, **b** 20, **c** 50, and **d** 100 wt% excess

describe the synthesis of $LaSrLiH_2O_2$ by a conventional solid-state reaction under ambient pressure and characterize its electrochemical properties.

The starting materials (which were identical to those used in the high-pressure method) were pelletized and placed in a sealed sample container made of stainless steel, with subsequent sintering performed at 650 °C for 6 h under H_2.

Figure 13.12 shows the X-ray diffraction patterns of $LaSrLiH_2O_2$ synthesized using different amounts of LiH (stoichiometric, 20, 50, and 100 wt% excess), with the main diffraction peaks corresponding to the space group of $LaSrLiH_2O_2$, i.e., *I*4/*mmm*. However, small diffraction peaks indexed to SrO, SrH_2, and/or La_2O_3, which were present in the raw starting materials, were observed for samples synthesized using a small excess or no excess of LiH (stoichiometric, 20 wt%, and 50 wt%). The amount of residual starting materials decreased as the amount of LiH increased, with $LaSrLiH_2O_2$ obtained as a single phase only at a 100 wt% excess. In addition, excess LiH improved the crystallinity of $LaSrLiH_2O_2$, i.e., the magnification of the normalized 004 peaks (Fig. 13.12) showed that their full width at half maximum decreased as the amount of LiH increased. Therefore, excess LiH not only prevented the loss of lithium and hydrogen during the synthesis of $LaSrLiH_2O_2$, but also acted as a flux for reducing the synthesis temperature.

Crystal structure analysis revealed that the sample prepared under ambient pressure had almost the same structure as the high-pressure one, with the refined site occupancies of each atom indicating that the former exhibited a nearly stoichiometric composition without vacancies. However, mixing of H^- and O in the 4*c* axial anion site (g(H1) = 0.9361(5) and g(O1) = 1 − g(H1)) in Li octahedra

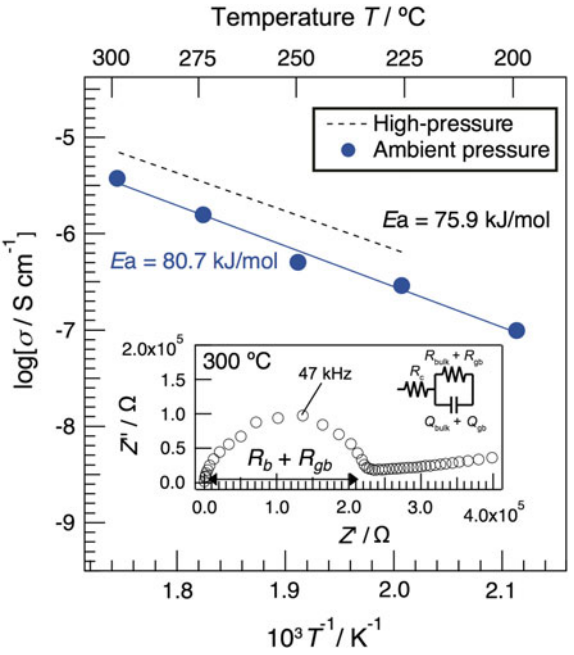

Fig. 13.13 Arrhenius and Cole-Cole plots of $LaSrLiH_2O_2$. The inset shows an equivalent circuit used to model impedance data

was detected for the ambient-pressure sample, whereas this site was exclusively occupied by H^- in the high-pressure sample.

The ionic conductivity of $LaSrLiH_2O_2$ synthesized at ambient pressure was evaluated by AC impedance measurements. The corresponding impedance and Arrhenius plots are shown in Fig. 13.13, with the conductivity of the high-pressure $LaSrLiH_2O_2$ synthesized in our previous study also plotted for comparison [6]. The impedance plot exhibited a typical form, comprising a semicircle in the high-frequency range and a spike in the low-frequency range, which corresponded to contributions of the bulk and grain boundary and the electrode, respectively. The former contribution was estimated by fitting impedance spectra using an equivalent circuit, as shown in Fig. 13.13. For the ambient-pressure sample, the activation energy of ionic conduction was calculated as 80.7 kJ mol^{-1}, which is nearly equal to that observed for the high-pressure sample [6]. The total conductivity (bulk + grain boundary) of the ambient-pressure sample was determined as 3.2×10^{-6} S cm^{-1} at 300 °C, slightly less than that of the high-pressure sample. Given the crystal structure of $LaSrLiH_2O_2$, in which tetragonal $(LiH_2)^-$ and $(LaSrO_2)^+$ layers are alternately stacked along the *c*-axis, the hydride ions were expected to exhibit two-dimensional diffusion in the LiH_4 plane. Hence, the movement of H^- in the crystal lattice of ambient-pressure $LaSrLiH_2O_2$ may have been inhibited by the presence of oxide ions in the $(LiH_2)^-$ layer.

Thus, we successfully synthesized $LaSrLiH_2O_2$ by a conventional solid-state reaction under ambient pressure [48], with a two-fold molar excess of LiH required to obtain single-phase $LaSrLiH_2O_2$. The sample synthesized at ambient pressure exhibited a crystal structure and H^- conductivity similar to those observed for the high-pressure sample, implying that the method described here should increase the applicability of H^- conductors as solid electrolytes.

13.4 Concluding Remarks

This chapter outlined the properties of ion conductors and material search methods, introducing Li^+ and H^- conductors and providing examples of material search (e.g., element substitution and structure-based methods). However, broader material variability will be required to fabricate viable electrochemical devices based on solid electrolytes, necessitating the utilization of composition-based material search, which is one of the conventional material discovery methods. The approach described is significantly influenced by the experience and intuition of researchers, and it generally takes longer than element substitution and structure-based methods. However, the recent development of theoretical calculation and material informatics methods is expected to shorten the time required [49–53], allowing high-speed screening of prospective compositions/structures. In some cases, this approach might be misleading, since not all theoretically predicted compositions or structures can be obtained by the present synthetic techniques, as exemplified by the failure of the composition/structure-based search in the case of Li^+ and H^- conductors. Thus, the area of materials informatics for composition-based material search is still in its infancy, but it holds promise for the future.

Acknowledgements This research was supported by JST, PRESTO, and Grant-in-Aid for Young Scientists (A) no. 15H05497 and (B) no. 24750209; Grant-in-Aid for Challenging Exploratory Research no. 15K13803, 23655191, and 25620180; and Grant-in-Aid for Scientific Research on Innovative Areas no. 25106005 and 25106009, from the Japan Society for the Promotion of Science. Synchrotron and neutron radiation experiments were carried out as four projects approved by the Japan Synchrotron Radiation Research Institute (JASRI) (proposals no. 2013A1704, 2015A1778, and 2015B1768), the Japan Proton Accelerator Research Complex (J-PARC) (proposal no. 2010A0058), the Spallation Neutron Source (SNS) in the Oakridge National Laboratory (proposal no. IPTS5808 and 10030), and the Neutron Scattering Program Advisory Committee of IMSS, KEK (proposal no. 2014S10). Part of the neutron experiments (proposal no. 2014S10) was performed at the BL09 Special Environment Neutron Powder Diffractometer (SPICA) developed by the Research and Development Initiative for Scientific Innovation of New Generation Batteries (RISING) project of the New Energy and Industrial Technology Development Organization (NEDO). Supercomputing time at the Academic Center for Computing and Media Studies (ACCMS) at Kyoto University is gratefully acknowledged. Further information regarding the materials and methods is included in the supplementary materials.

References

1. B.B. Owens, G.R. Argue, Science **157**, 308 (1967)
2. T. Takahashi, O. Yamamoto, S. Yamada, S. Hayashi, J. Electrochem. Soc. **126**, 1654 (1979)
3. T. Takahashi, R. Kanno, Y. Takeda, O. Yamamoto, Solid State Ion. **3**, 283 (1981)
4. N. Kamaya, K. Homma, Y. Yamakawa, M. Hirayama, R. Kanno, M. Yonemura, T. Kamiyama, Y. Kato, S. Hama, K. Kawamoto, A. Mitsui, Nat. Mater. **10**, 682 (2011)
5. Y. Kato, S. Hori, T. Saito, K. Suzuki, M. Hirayama, A. Mitsui, M. Yonemura, H. Iba, R. Kanno, Nat. Energy **1**, 16030 (2016)
6. G. Kobayashi, Y. Hinuma, S. Matsuoka, A. Watanabe, M. Iqbal, M. Hirayama, M. Yonemura, T. Kamiyama, I. Tanaka, R. Kanno, Science **351**, 1314 (2016)
7. M.C. Verbraeken, C. Cheung, E. Suard, J.T.S. Irvine, Nat. Mater. **14**, 95 (2015)
8. V. Thangadurai, S. Narayanan, D. Pinzaru, Chem. Soc. Rev. **43**, 4714 (2014)
9. U.V. Alpen, M.F. Bell, W. Wichelhaus, K.Y. Cheung, G.J. Dudley, Electrochim. Acta **23**, 1395 (1978)
10. Y. Inaguma, L. Chen, M. Itoh, T. Nakamura, Solid State Ion. **70–71** Part 1, 196 (1994)
11. V. Thangadurai, H. Kaack, W.J.F. Weppner, J. Am. Ceram. Soc. **86**, 437 (2003)
12. A. Hayashi, S. Hama, H. Morimoto, M. Tatsumisago, T. Minami, Chem. Lett. **30**, 872 (2001)
13. R. Kanno, M. Murayama, J. Electrochem. Soc. **148**, A742 (2001)
14. K. Minami, A. Hayashi, M. Tatsumisago, J. Am. Ceram. Soc. **94**, 1779 (2011)
15. T. Phraewphiphat, M. Iqbal, K. Suzuki, Y. Matsuda, M. Yonemura, M. Hirayama, R. Kanno, J. Solid State Chem. **225**, 431 (2015)
16. Y. Sun, K. Suzuki, S. Hori, M. Hirayama, R. Kanno, Chem. Mater. **29**, 5858 (2017)
17. R. Kanno, T. Hata, Y. Kawamoto, M. Irie, Solid State Ion. **130**, 97 (2000)
18. Y. Inoue, K. Suzuki, N. Matsui, M. Hirayama, R. Kanno, J. Solid State Chem. **246**, 334 (2017)
19. Y. Inaguma, C. Liquan, M. Itoh, T. Nakamura, T. Uchida, H. Ikuta, M. Wakihara, Solid State Commun. **86**, 689 (1993)
20. Y. Inaguma, T. Katsumata, M. Itoh, Y. Morii, T. Tsurui, Solid State Ion. **177**, 3037 (2006)
21. G. Zhao, I. Muhammad, K. Suzuki, M. Hirayama, R. Kanno, Mater. Trans. **57**, 1370 (2016)
22. E.E. Hellstrom, W. Van Gool, Solid State Ion. **2**, 59 (1981)
23. C.J.M. Rooymans, Z. Anorg, Allg. Chem. **313**, 234 (1961)
24. M. Tabuchi, S. Tsutsui, C. Masquelier, R. Kanno, K. Ado, I. Matsubara, S. Nasu, H. Kageyama, J. Solid State Chem. **140**, 159 (1998)
25. A.F. Andresen, A.J. Maeland, D. Slotfeldt-Ellingsen, J. Solid State Chem. **20**, 93 (1977)
26. B. Wegner, R. Essmann, J. Bock, H. Jacobs, P. Fischer, Eur. J. Solid State Inorg. Chem. **29**, 1217 (1992)
27. F. Altorfer, W. Buhrer, B. Winkler, G. Coddens, R. Essmann, H. Jacobs, Solid State Ion. **70–71**, 272 (1994)
28. B. Zhu, X. Yang, Electrochem. Commun. **1**, 411 (1999)
29. B. Zhu, X. Liu, Electrochem. Commun. **2**, 10 (2000)
30. F.W. Poulsen, Solid State Ion. **145**, 387 (2001)
31. M.C. Verbraeken, E. Suard, J.T.S. Irvine, J. Mater. Chem. **19**, 2766 (2009)
32. R.M. Helps, N.H. Rees, M.A. Hayward, Inorg. Chem. **49**, 11062 (2010)
33. Y. Kobayashi, O.J. Hernandez, T. Sakaguchi, T. Yajima, T. Roisnel, Y. Tsujimoto, M. Morita, Y. Noda, Y. Mogami, A. Kitada, M. Ohkura, S. Hosokawa, Z. Li, K. Hayashi, Y. Kusano, J.E. Kim, N. Tsuji, A. Fujiwara, Y. Matsushita, K. Yoshimura, K. Takegoshi, M. Inoue, M. Takano, H. Kageyama, Nat. Mater. **11**, 507 (2012)
34. T. Sakaguchi, Y. Kobayashi, T. Yajima, M. Ohkura, C. Tassel, F. Takeiri, S. Mitsuoka, H. Ohkubo, T. Yamamoto, J.E. Kim, N. Tsuji, A. Fujihara, Y. Matsushita, J. Hester, M. Avdeev, K. Ohoyama, H. Kageyama, Inorg. Chem. **51**, 11371 (2012)
35. H. Schwarz, Ph.D. Thesis, University of Karlsruhe, 1991

36. J. Bang, S. Matsuishi, H. Hiraka, F. Fujisaki, T. Otomo, S. Maki, J.-I. Yamaura, R. Kumai, Y. Murakami, H. Hosono, J. Am. Chem. Soc. **136**, 7221 (2014)
37. M.A. Hayward, E.J. Cussen, J.B. Claridge, M. Bieringer, M.J. Rosseinsky, C.J. Kiely, S.J. Blundell, I.M. Marshall, F.L. Pratt, Science **295**, 1882 (2002)
38. K. Hayashi, S. Matsuishi, T. Kamiya, M. Hirano, H. Hosono, Nature **419**, 462 (2002)
39. K. Hayashi, P.V. Sushko, A.L. Shluger, M. Hirano, H. Hosono, J. Phys. Chem. B **109**, 23836 (2005)
40. S. Matsuishi, K. Hayashi, M. Hirano, H. Hosono, J. Am. Chem. Soc. **127**, 12454 (2005)
41. C.G. Van de Walle, Phys. Rev. Lett. **85**, 1012 (2000)
42. C.G. Van de Walle, J. Neugebauer, Nature **423**, 626 (2003)
43. J. Zhang, G. Gou, B. Pan, J. Phys. Chem. C **118**, 17254 (2014)
44. J.P. Attfield, G. Férey, J. Solid State Chem. **80**, 112 (1989)
45. B.J. Neudecker, W. Weppner, J. Electrochem. Soc. **143**, 2198 (1996)
46. N. Kamaya, K. Homma, Y. Yamakawa, M. Hirayama, R. Kanno, M. Yonemura, T. Kamiyama, Y. Kato, S. Hama, K. Kawamoto, A. Mitsui, Nat. Mater. **10**, 682 (2011)
47. A. San-Martin, F.D. Manchester, Bull. Alloy Phase Diagrams **8**, 30 (1987)
48. A. Watanabe, G. Kobayashi, N. Matsui, M. Yonemura, A. Kubota, K. Suzuki, M. Hirayama, R. Kanno, Electrochemistry **85**, 88 (2017)
49. M. Nishijima, T. Ootani, Y. Kamimura, T. Sueki, S. Esaki, S. Murai, K. Fujita, K. Tanaka, K. Ohira, Y. Koyama, I. Tanaka, Nat. Commun. **5**, 4553 (2014)
50. Y. Hinuma, T. Hatakeyama, Y. Kumagai, L.A. Burton, H. Sato, Y. Muraba, S. Iimura, H. Hiramatsu, I. Tanaka, H. Hosono, F. Oba, Nat. Commun. **7**, 11962 (2016)
51. A.D. Sendek, Q. Yang, E.D. Cubuk, K.-A.N. Duerloo, Y. Cui, E.J. Reed, Energy Environ. Sci. **10**, 306 (2017)
52. W.D. Richards, Y. Wang, L.J. Miara, J.C. Kim, G. Ceder, Energy Environ. Sci. **9**, 3272 (2016)
53. A. Seko, H. Hayashi, K. Nakayama, A. Takahashi, I. Tanaka, Phys. Rev. B **95**, 144110 (2017)